# Accurate formula for the effective conductivity of highly clustered two-phase materials

Murray Skolnick
*Department of Chemistry, Princeton University, Princeton, New Jersey 08544, USA*

Salvatore Torquato*
*Department of Chemistry, Department of Physics, Princeton Materials Institute, and Program in Applied and Computational Mathematics, Princeton University, Princeton, New Jersey 08544, USA*

(Received 27 January 2025; accepted 28 April 2025; published 8 May 2025)

Two-phase heterogeneous materials arising in a variety of natural and synthetic situations exhibit a wide variety of microstructures and thus display a broad spectrum of effective physical properties. Given that such properties of disordered materials generally depend on an infinite set of microstructural correlation functions that are typically unobtainable, in practice, theoretical approaches must rely on rigorous bounds and approximations on the effective properties that depend on a limited set of nontrivial microstructural information. Torquato [*Random Heterogeneous Materials, Microstructure and Macroscopic Properties* (Springer-Verlag, New York, 2002)] derived such an approximation for the effective thermal/electrical conductivity of two-phase microstructures that perturb about those that realize the well-known self-consistent formula, a key feature of such microstructures being phase-inversion symmetry which can be observed in certain cellular, bicontinuous, and porous materials. Here, we show via extensive numerical simulations that this virtually unexamined approximation, which depends on up to three-point correlations functions, accurately predicts the effective conductivities of various two- and three-dimensional two-phase microstructures across phase volume fractions in which both phases can form large and well-connected clusters, including certain phase-inversion symmetric microstructures as well as phase-inversion asymmetric dispersions of certain fully penetrable particles. We also highlight the accurate sensitivity of this approximation to phase-connectedness properties by showing that it predicts percolation thresholds that are in good quantitative and/or qualitative agreement with known thresholds for the models considered here. Finally, we discuss how this formula can be used to design materials with desirable effective conductivity properties and thus aid in materials by design.

DOI: 10.1103/PhysRevMaterials.9.055601

## I. INTRODUCTION

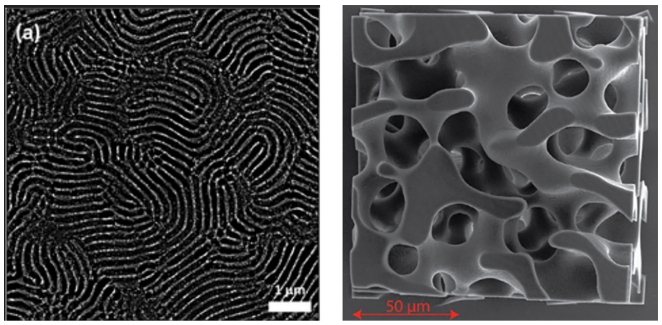
Disordered heterogeneous two-phase materials in $d$-dimensional Euclidean space $\mathbb{R}^d$ abound in natural and synthetic situations; examples include composites, polymer blends, colloids, porous media, biological media, and complex fluids [1–8]. Among the broad spectrum of realizable microstructure phase geometries and topologies, the microstructures of certain two-phase materials like aerogels [9,10], interpenetrating cermets [11–13], and those derived from triply periodic minimal surfaces [14–16] consist of large and well-connected clusters of both phases. Examples of real material microstructures with such phase geometries and topologies are the labyrinth of silicon nano walls [17] shown in Fig. 1(a) and the spinodal architected metamaterial [18] shown in Fig. 1(b).

In general, the effective physical properties of heterogeneous materials depend on an infinite set of correlation functions [1,21–24]. For example, there is the countably infinite set of the standard $n$-point correlation functions $S_n^{(i)}(\mathbf{x}_1, ..., \mathbf{x}_n)$ $(n = 1, 2, 3, \ldots)$, which gives the probability of finding the points $\mathbf{x}_1, ..., \mathbf{x}_n$ in phase $i = 1, 2$ for two-phase materials [1]. Since infinite sets of correlation functions are typically unobtainable in practice, it is desirable to incorporate nontrivial lower-order correlation functions to obtain useful theoretical estimates of the effective properties via rigorous bounds and/or approximations [1,3,24,25]. One such theoretical technique for predicting effective properties (i.e., conductivity and elastic moduli) is the strong-contrast expansion whose terms consist of functionals of certain field quantities and $S_n^{(i)}(\mathbf{x}_1, ..., \mathbf{x}_n)$ for all $n$ [1,21,26–31]. Importantly, by utilizing an expansion parameter that is a rational function of the phase properties, rather than simple differences of them, the strong-contrast expansions possess superior convergence properties for any phase property contrast ratio. Moreover, lower-order truncation of this rapidly converging series results in accurate approximations on the effective conductivity and elastic moduli for various classes of microstructures because they approximate higher-order terms accurately, as we will now describe.

As the aforementioned approximations incorporate microstructural information up to the level of the three-point correlation function $S_3$, they are sometimes referred to as *three-point approximations* [1]. For example, the three-point approximation for the effective conductivity $\sigma_e$ for dispersions

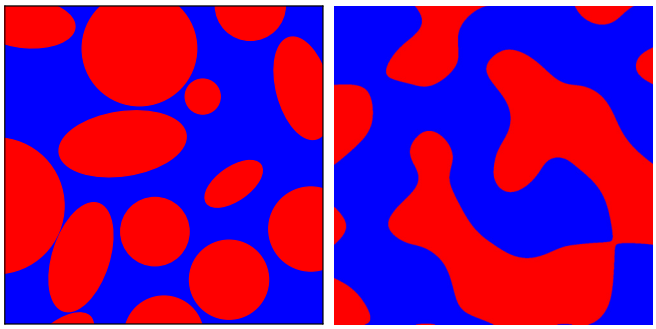
*Contact author: torquato@electron.princeton.edu

 ©2025 American Physical Society




(a) (b)

FIG. 1. Images of real material microstructures in which both phases form well-connected clusters and likely possess phase-inversion symmetry: (a) Scanning electron microscope (SEM) image of a labyrinth of silicon nano walls (light gray) and void (black) manufactured via solvent vapor annealing using a self-assembled block copolymer template [17]. This particular system likely has silicon phase volume fraction $\phi_2 \approx 0.5$. (b) SEM image of a spinodal architected metamaterial manufactured using two-photon polymerization direct laser writing which has solid phase-volume fraction $\phi_2 = 0.30$ [18]. The microstructure shown in (a) appears to be phase-inversion symmetric since the geometries and topologies of its silicon and void phases are qualitatively similar to one another. The two-phase microstructure shown in (b) is likely phase-inversion symmetric since it was derived from a level cut of a concentration field simulated via the Cahn-Hilliard equation [18], which treats the interactions between and dynamics of the separating phases identically [19,20]. The image in (a) is licensed under Creative Commons BY 4.0. The image in (b) is reprinted from Ref. [18] with permission from Elsevier.



(a) (b)

FIG. 2. Schematics illustrating the distinct classes of microstructures for which the different three-point strong-contrast approximations (1) and (3) are accurate. The dispersion shown in (a) consists of nonoverlapping particles (red) embedded in a matrix (blue), while the microstructure shown in (b) consists of amorphous inclusions of both the red and blue phases. The approximation in Eq. (1) is highly accurate for microstructures like that shown in (a) in which one phase does do not form large clusters. By contrast, as we will show in this paper, approximation (3) is accurate for microstructures resembling that shown in (b) in which both phases can form large clusters.

of particles in a matrix is given by [26]

$$\frac{\sigma_e}{\sigma_q} = \frac{\left[1 + (d-1)\phi_p \beta_{pq} - (d-1)\phi_1 \zeta_p \beta_{pq}^2\right]}{1 - \phi_p \beta_{pq} - (d-1)\phi_q \zeta_p \beta_{pq}^2}, \tag{1}$$

in which

$$\beta_{pq} = \frac{\sigma_p - \sigma_q}{\sigma_p + (d-1)\sigma_q} \tag{2}$$

is the scalar polarizability, $\sigma_p$ ($\sigma_q$) is the conductivity of phase $p$ ($q$), and the three-point parameter $\zeta_p$ is a functional over $S_1$, $S_2$, and $S_3$ (see Sec. II for additional details). Approximation (1) is highly accurate for dispersions in which the particles (phase 2) generally do not form large clusters [1,21,26,27,32]. A schematic image illustrating the class of dispersions for which approximation (1) is accurate is shown in Fig. 2(a). Formula (1) has been shown to accurately predict the effective thermal/electrical conductivities of various disordered packings of disks and spheres [33,34], random packings of ellipsoids and Platonic solids [35], and by mathematical analogy, the effective diffusion coefficients of certain chromatography columns whose microstructures consist of disordered packings of spherical beads [36–38].

Torquato [1] derived a different, virtually unexplored, three-point strong-contrast approximation for the effective conductivity that was designed to predict $\sigma_e$ for a structurally distinct class of two-phase material microstructures in which both phases can form large and well-connected clusters, including *bicontinuous* [39] systems, across volume fractions, which is given by

$$\phi_2 \frac{\sigma_e + (d-1)\sigma_1}{\sigma_e - \sigma_1} + \phi_1 \frac{\sigma_e + (d-1)\sigma_2}{\sigma_e - \sigma_2} = 2 - d - (d-1)\beta_{21}\left[\phi_1 \zeta_2 - \frac{\phi_2(1-\zeta_2)}{1 + (d-2)\beta_{21}}\right]. \tag{3}$$

A schematic image illustrating the class of highly clustered microstructures for which approximation (3) can be applied is shown in Fig. 2(b). In this paper, we initiate a program to examine the accuracy of this approximation using comprehensive numerical simulations. Torquato [1] predicted that this formula would be accurate for microstructures that resemble those that realize the well-known self-consistent formula, a key feature of which is phase-inversion symmetry. In such phase-inversion symmetric microstructures, like the nanowall labyrinth and spinodal architected metamaterial microstructures shown in Fig. 1, the morphology of phase 1 at volume fraction $\phi_1$ is statistically identical that of phase 2 in the system where the volume fraction of phase 1 is $1 - \phi_1$ [1] (see Sec. III for additional details).

Beyond being phase-inversion symmetric, we note that microstructures that realize the self-consistent formula also have a nontrivial percolation threshold (i.e., the critical volume fraction at which phase 2 forms a sample-spanning cluster) $\phi_{2c} = 1/d$ and will be bicontinuous in three dimensions (3D) for $\frac{1}{3} < \phi_2 < \frac{2}{3}$ [1]. Since microstructures with percolation thresholds at intermediate volume fractions necessarily possess large clusters away but near the thresholds, we anticipate that formula (3) should also be accurate for highly clustered two-phase materials, phase-inversion symmetric or not, which we verify below. Note that Torquato's complete derivation of Eq. (3) using strong-contrast expansions as well as a detailed discussion on how it perturbs about the self-consistent formula are provided in Ref. [1]. Henceforth, we refer to approximation (3) as the *self-consistent strong-contrast approximation* which, by mathematical analogy, can also be used

to compute the effective diffusion coefficient $D_e$, dielectric constant $\epsilon_e$, and the magnetic permeability $\mu_e$ of two-phase materials [1].

We demonstrate the high predictive power of the self-consistent strong-contrast approximation (3) by comparing its predictions for $\sigma_e$ to those obtained via simulations for several physically realistic disordered model two-dimensional (2D) and 3D microstructures that exhibit phase clustering across volume fractions. We specifically consider phase-inversion symmetric Debye random media [40,41] and symmetric-cell materials (see Sec. II for definitions) with square and cubical cells [1] as well as phase-inversion asymmetric dispersions of fully penetrable disks, spheres, elongated ellipses, and oblate ellipsoids [1]. Beyond accurate predictions for $\sigma_e$, we also derive from Eq. (3) nontrivial predictions for $\phi_{2c}$ that depend on microstructural information via the parameter $\zeta_2$. We show that these predicted percolation thresholds are in good qualitative and/or quantitative agreement with known values of $\phi_{2c}$ for the models considered here. We further highlight the sensitivity of Eq. (3) to microstructure percolation properties by examining it as a function of phase conductivity contrast ratio $\sigma_2/\sigma_1$ across all volume fractions.

The rest of the paper is organized as follows: Information about the three-point parameter $\zeta_p$ is provided in Sec. II. The model microstructures, their values of the three-point parameters across volume fractions, and phase-inversion symmetry/asymmetry are summarized in Sec. III. The main results are presented in Sec. IV, and conclusions and future directions are discussed in Sec. V.

## II. THE THREE-POINT PARAMETER $\zeta_p$

Here, we summarize key details about the three-point microstructural parameter $\zeta_p$ that appears in approximations (1) and (3). We note that $\zeta_p$ also arises in rigorous bounds on the effective conductivity and the elastic moduli that improve upon the well-known Hashin-Shtrikman bounds [26,42–53], strong-contrast expansions truncated after third order for the effective elastic moduli [1,27], as well as an approximation for the fluid permeability of certain materials [16,54,55]. The parameter $\zeta_p$ for phase $p$ of a two-phase microstructure is specifically given by

$$\zeta_p = \frac{4}{\pi\phi_1\phi_2}\int_0^\infty \frac{dr}{r}\int_0^\infty \frac{ds}{s}\int_0^\pi d\theta\cos(2\theta) \times\left[S_3^{(p)}(r,s,\theta) - \frac{S_2^{(p)}(r)S_2^{(p)}(s)}{S_1^{(p)}}\right], \tag{4}$$

for 2D systems, and by

$$\zeta_p = \frac{9}{2\phi_1\phi_2}\int_0^\infty \frac{dr}{r}\int_0^\infty \frac{ds}{s}\int_{-1}^1 d(\cos\theta)P_2(\cos\theta) \times\left[S_3^{(p)}(r,s,\theta) - \frac{S_2^{(p)}(r)S_2^{(p)}(s)}{S_1^{(p)}}\right]. \tag{5}$$

for 3D ones [56]. The quantities $S_1^{(p)}$, $S_2^{(p)}(r)$, and $S_3^{(p)}(r,s,\theta)$ are, respectively, the probabilities of finding in phase $p$ a single point, the end points of a line segment of length $r$, and the vertices of a triangle with two sides of length $r$, $s$, and angle $\theta$ between them. In the integral in Eq. (5), $P_2$ is the Legendre polynomial of order 2. Note that $S_1^{(p)}$ is simply the volume fraction of phase $p$, $\phi_p$, and that $0 \leqslant \zeta_p \leqslant 1$ and $\zeta_1 + \zeta_2 = 1$. As the three-point correlation function $S_3^{(p)}$ is generally not known analytically for most microstructures [1,26,57–61], the parameter $\zeta_p$ must be ascertained directly from microstructural samples using numerical methods. We recently developed such a method for computing $\zeta_p$ that improves upon the accuracy and computational performance of previous methods [34] which we employ in this paper as described in Sec. III B.

We recently showed via comprehensive numerical simulations that $\zeta_2$ tends to be larger for microstructures in which phase 2 is more well connected and ramified for a given value of $\phi_2$ [34]. Symmetric-cell materials, which are constructed by partitioning space into cells of arbitrary size and shape and then randomly designating them as phases 1 and 2 with respective probabilities $\phi_1$ and $\phi_2$ [1,62], specifically have

$$\zeta_2 = \phi_2 + (1-2\phi_2)g, \tag{6}$$

in which $0 \leqslant g \leqslant 1$ is a parameter that depends on the cell shape and is thus referred to as the *cell-shape parameter*. Specifically, $g$ is a functional over a certain three-point statistical quantity associated with the cell geometry [1]. By virtue of their construction, all symmetric-cell materials are phase-inversion symmetric [1]. One can show that such materials with circular/spherical cells have shape parameter $g = 0$, while those with needlelike cells in 2D and disk-shaped cells in 3D have $g = 1$ [1]. We note that space can be tessellated by polydisperse circles/spheres or ellipses/ellipsoids which necessarily must have a continuous range of sizes ranging to the infinitesimally small. Moreover, Kim and Torquato [63,64] recently showed that such multiscale tessellations of disks and spheres can be effectively realized computationally using a tessellation-based procedure. Finally, Eq. (6) implies that all symmetric-cell materials have $\zeta_2 = \frac{1}{2}$ for $\phi_2 = \frac{1}{2}$ which is a general property of all phase-inversion symmetric microstructures for reasons detailed in Ref. [1].

## III. MODEL MICROSTRUCTURES AND THREE-POINT PARAMETERS

In this section, we summarize the salient details of the four model 2D and 3D microstructures that we use as benchmarks to demonstrate the accuracy of the self-consistent strong-contrast approximation in Eq. (3). By virtue of their construction, these microstructures all exhibit much greater degrees of phase clustering than that observed in dispersions of well-separated particles in a matrix for a given volume fraction. We also compute their respective three-point parameters $\zeta_2$ across volume fractions and show how one can extract cell-shape parameters $g$ from these data for Debye random media and thus interpret these microstructures as effective symmetric-cell materials.

### A. Models

We specifically consider symmetric-cell materials with square and cubical cells with side length $a$. These microstructures have two-point correlation functions

$S_2^{(p)}(r) = \phi_p\phi_q W_2(r;a) + \phi_p^2$ in which $W_2(r;a)$ is the single-cell weight function for which exact expressions are given in Ref. [1]. As these microstructures are sometimes referred to as *random checkerboards*, we use the acronym RCB to refer to them henceforth. Here, the RCB microstructures serve as a convenient platform to test the accuracy of Eq. (3) for symmetric-cell microstructures, as they are single scale, and thus, generating realizations of them and ascertaining their effective conductivities is computationally straightforward. We also examine so-called Debye random media (DRM) which are phase-inversion symmetric [65,66] models of two-phase media that are defined entirely by the two-point correlation function $S_2^{(p)}(r) = \phi_p\phi_q \exp(-r/a) + \phi_p^2$ in which $a > 0$ is the characteristic length scale of the microstructure. Such an exponential form of $S_2(r)$ was hypothesized by Debye *et al.* [40] to model 3D microstructures with phases of "fully random shape, size, and distribution" and were shown to be realizable in 2D [41] and 3D [54]. Note that DRM have been shown to be a good approximation of certain microstructures, including Fontainebleau sandstone [67], snow [68], and certain mesoporous materials [69].

We also consider dispersions of fully penetrable disks, spheres, as well as randomly oriented ellipses and oblate ellipsoids [1]. Fully penetrable disk/sphere (FPD/S) systems are prepared by decorating the points of a Poisson point process with radius $a$ disks/spheres that are free to overlap with one another. The volume fraction of the matrix phase of these systems is given by $\phi_1 = \exp[-\rho v_1(a)]$, in which $\rho$ is the number density of the underlying Poisson point pattern and $v_1(a)$ is the volume of a $d$-dimensional sphere of radius $a$ [1,70]. The two-point function for the matrix phase of these microstructures is given by $S_2^{(1)} = \exp[-\ln\phi_1 v_2(r;a)/v_1(a)]$, in which $v_2(r;a)$ is the union volume of two $d$-dimensional spheres of radius $a$ whose centers are a distance $r$ apart. The model fully penetrable ellipse/ellipsoid (FPE/E) systems are prepared like the disk/sphere systems, except that each particle is given a random orientation in space. Their $\phi_1$ and $S_2^{(1)}$ are also mathematically analogous to those of the FPD/S systems [1,70]. Note that the aforementioned systems are realistic models of consolidated media such as sandstones and sintered materials [71]. Sample images of microstructures of these four highly clustered models in 3D with $\phi_2 = \frac{1}{2}$ are shown in Fig. 3.

By definition, a phase-inversion symmetric microstructure is one in which the $n$-point correlation functions for phases 1 and 2 obey the following relation [1]:

$$S_n^{(1)}(\mathbf{x}^n;\phi_1,\phi_2) = S_n^{(2)}(\mathbf{x}^n;\phi_2,\phi_1), \quad n \geqslant 2. \tag{7}$$

Note that the RCB and Debye microstructures have two-point correlation functions that satisfy Eq. (7) for $n = 2$, and thus, they possess phase-inversion symmetry at the two-point level. We show in Sec. III B that these models are also phase-inversion symmetric at the three-point level. By contrast, the two-point correlation functions for the fully penetrable particle models do not satisfy Eq. (7) and, as we will show in Sec. III B, these models are also not phase-inversion symmetric at the three-point level [72].

For subsequent calculations, we specifically consider 2D $1024 \times 1024$ pixel and 3D $192 \times 192 \times 192$ voxel realizations of the RCB microstructures. The 2D and 3D RCB systems have $a = 8$ and 6, respectively, and were made using a random number generator. The Debye microstructures are the same size as the RCB systems but have characteristic length scales $a = 10$ in 2D and $a = 5$ in 3D. Note that the ratio of major to minor axes $b/a = 5$ for the FPE/E systems. Additional details concerning the generation of the Debye and fully penetrable particle microstructures are provided in Ref. [34].

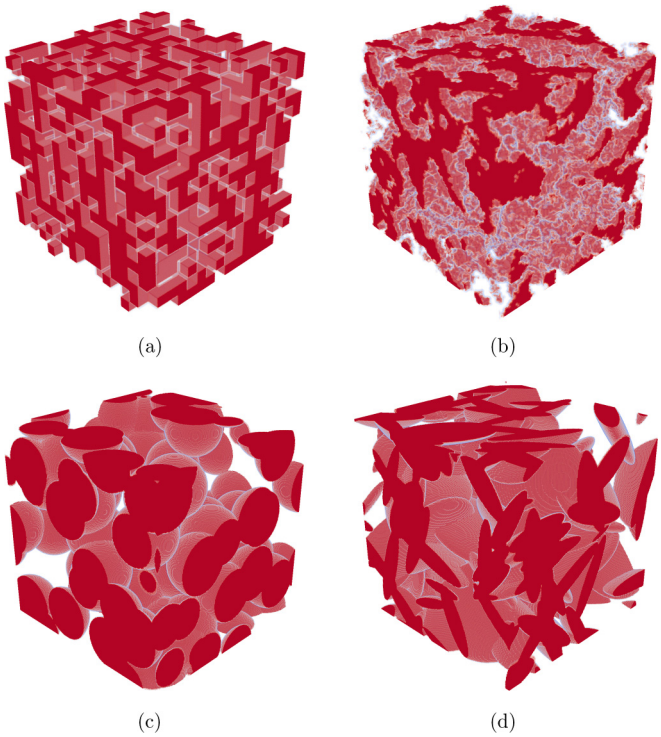



FIG. 3. Sample images of the model highly clustered microstructures considered in this paper: (a) random checkerboard, (b) Debye random media, as well as fully penetrable (c) spheres and (d) oblate ellipsoids. The images shown in (a)–(d) correspond to $\frac{1}{8}$th of the total volume of the microstructures used in the calculations and have phase 2 (red) volume fraction $\phi_2 = \frac{1}{2}$. To facilitate visualization of the microstructure, phase 1 is transparent in these images.

### B. Results for three-point parameters

Before testing Eq. (3) on the aforementioned model microstructures, we first examine their values of $\zeta_2$. It is seen that the parameters $\zeta_2$ for all four models vary linearly with $\phi_2$ in the plots of $\zeta_2$ vs $\phi_2$ in Fig. 4. Note that, for the penetrable particle models, we take the particles to be phase 2 and the matrix as phase 1. Additionally, we note that DRM have $\zeta_2 = 0.5 \pm 0.001$, implying that they must also possess phase-inversion symmetry at the three-point level. By contrast, the phase-inversion asymmetric fully penetrable particle models both have $\zeta_2 \neq \frac{1}{2}$.

Since the three-point parameter $\zeta_2$ for 2D and 3D DRM varies linearly with respect to $\phi_2$ and is equal to $\frac{1}{2}$ when $\phi_2 = \frac{1}{2}$, we can fit Eq. (6) to these data to extrapolate effective cell-shape parameters $g$ for these models. We specifically find from these fits that $g_{\mathrm{DRM}}^{(2\mathrm{D})} = 0.2487$ and $g_{\mathrm{DRM}}^{(3\mathrm{D})} = 0.2643$.

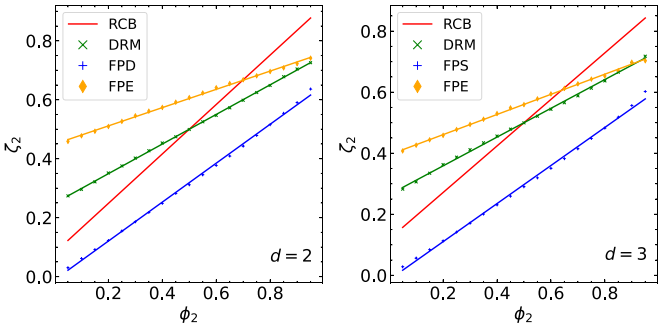



FIG. 4. Plots of the three-point parameter $\zeta_2$ as a function of phase 2 volume fraction $\phi_2$ for the model microstructures in (a) 2D and (b) 3D. The scatter plots for Debye random media as well as the fully penetrable particle models correspond to ensemble averaged values of $\zeta_2$ computed via Monte Carlo integration [34], while the corresponding solid lines are of linear regression fits (all with $R^2 > 0.999$) of the aforementioned numerical data. Values of $\zeta_2$ for the random checkerboards were obtained using previously calculated values of the cell-shape parameter $g$ for squares and cubes [1]. Every value of $\zeta_2$ for a given volume fraction was averaged over 20 different configurations. Error bars for the simulated data have been omitted, as they are not appreciable on the scale of this figure.

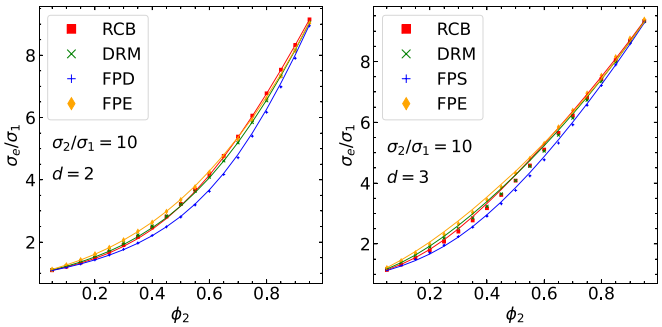



FIG. 5. Plots of the scaled effective conductivity $\sigma_e/\sigma_1$ as a function of phase 2 volume fraction $\phi_2$ for $\sigma_2/\sigma_1 = 10$ for the model microstructures in (a) 2D and (b) 3D. The scatter plots and solid lines correspond to simulation data and the formula in Eq. (3), respectively. Overall, we observe excellent agreement between predictions of Eq. (3) and the simulated data. Each simulated value of $\sigma_e$ for a given $\phi_2$ was averaged over 20 different configurations. Error bars for the simulation data have been omitted, as they are not appreciable on the scale of this figure. Simulated values of $\sigma_e$ for 2D and 3D Debye random media, random checkerboards, as well as the fully penetrable sphere and oblate ellipsoid systems were obtained via the fast Fourier transform (FFT)-based homogenization code described in Ref. [74]. Those for the fully penetrable disk and ellipse models were obtained using finite element methods in COMSOL Multiphysics.

While $g_{\rm DRM}^{(2D)}$ and $g_{\rm DRM}^{(3D)}$ are quite different from those of the RCB models (i.e., $g_{\rm RCB}^{(2D)} = 0.0808$ and $g_{\rm RCB}^{(3D)} = 0.1188$ [1]), they are respectively comparable to the $g$ values of 2D symmetric-cell materials with aspect ratio $\sim$2.9 elliptical cells and 3D symmetric-cell materials with needlelike cells [1]. Since DRM can be realized by certain space tessellations in 2D [73], it is reasonable that this model is an effective symmetric-cell microstructure.

## IV. PREDICTIONS OF THE SELF-CONSISTENT STRONG-CONTRAST APPROXIMATION

In this section, we demonstrate the accurate predictive power of the self-consistent strong-contrast approximation (3) for the effective conductivity $\sigma_e$ across phase volume fractions and conductivity contrast ratios $\sigma_2/\sigma_1$. We also derive from Eq. (3) formulas for the effective conductivity in the superconducting and insulating limits, i.e., $\sigma_2/\sigma_1 = \infty$ and $\sigma_2/\sigma_1 = 0$, respectively. Finally, we extract from these formulas accurate approximations for the percolation thresholds that incorporate three-point microstructural information via the parameter $\zeta_2$.

### A. Comparison to simulations

For the 2D and 3D models considered here, the predictions of approximation (3) for the effective conductivity overall agree well with simulated values obtained across all volume fractions for a moderate contrast ratio $\sigma_2/\sigma_1 = 10$, as seen in the plots of $\sigma_e$ vs $\phi_2$ in Fig. 5. In particular, the percent error $(100\% \times [\sigma_e^{(\rm theory)} - \sigma_e^{(\rm simulation)}]/\sigma_e^{(\rm simulation)})$ is between $-0.3$ and 3.4% in 2D and $-5.0$ and 1.0% in 3D. The slightly larger percent error for the 3D models is attributable to certain limitations on the parameter $\zeta_2$ in approximation (3) for 3D systems which are detailed in Appendix A. We recently showed that the self-consistent strong-contrast approximation (3) is accurate for DRM and, based on Torquato's original arguments [1], attributed this accuracy to the fact that this model is phase-inversion symmetric [34]. We also showed in that work that Eq. (3) is accurate for the fully penetrable particle models which we attributed to certain geometrical and topological similarities between these models and Debye random media [34]. To gain a more quantitative understanding of this observed accuracy of Eq. (3) for these highly clustered microstructures across volume fractions, we examine in Secs. IV B and IV C its predictions for $\sigma_e$ as a function of phase conductivity contrast ratio $\sigma_2/\sigma_1$ across volume fractions.

### B. Theoretical predictions across contrast ratios

We have established the high predictive power of approximation (3) with numerical simulations for a fixed contrast ratio of 10 across volume fractions for a variety of 2D and 3D models, implying its accuracy to predict values of $\sigma_e$ across all possible contrast ratios (i.e., $0 \leqslant \sigma_2/\sigma_1 \leqslant \infty$) without relying on computationally expensive numerical simulations that become increasingly challenging when the contrast ratios become very large or very small. The accurate sensitivity of formula (3) to phase connectedness information of 2D and 3D microstructures across volume fractions is highlighted in the plots of $\sigma_e$ as a function of contrast ratio $\sigma_2/\sigma_1$ across volume fractions for DRM in Fig. 6. Specifically, it is seen that Eq. (3) transitions from plateauing to constant values to power-law growth in $\sigma_2/\sigma_1$ at volume fractions $\phi_2 = 0.5$ and $\phi_2 = 0.182$ in 2D and 3D, respectively. Thus, Eq. (3) predicts that phase 2 forms percolating clusters at these respective volume fractions for 2D and 3D DRM. To investigate how Eq. (3) incorporates

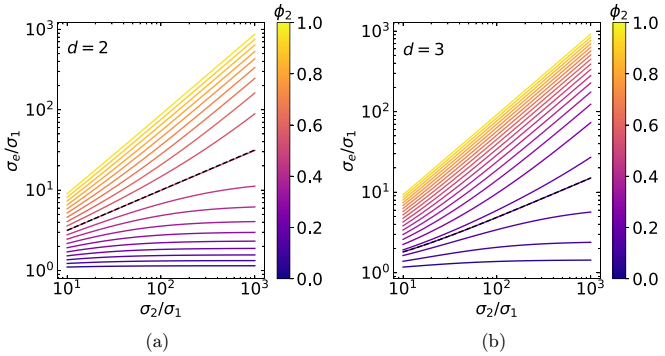



FIG. 6. Log-log plots of the scaled effective conductivity $\sigma_e/\sigma_1$ as a function of phase conductivity contrast ratio $\sigma_2/\sigma_1$ as predicted by Eq. (3) for Debye random media in (a) 2D and (b) 3D. Curves for different phase 2 volume fractions $\phi_2$ are color coded according to the legends on the right. In (a), the dashed black line is of Dykhne's exact formula $\sigma_e = \sqrt{\sigma_1\sigma_2}$ for 2D phase-inversion symmetric microstructures with $\phi_2 = \frac{1}{2}$ [75], which coincides with Eq. (3) for $\phi_2 = \frac{1}{2}$, $\zeta_2 = \frac{1}{2}$, and $d = 2$. In (b), the dashed black line highlights the effective conductivity of 3D DRM for $\phi_2 = 0.182$, the phase 2 percolation threshold for this model predicted by Eq. (10) using the effective cell-shape parameter $g_{\rm DRM}^{(3D)}$ for this microstructure computed in Sec. III B.

such nontrivial percolation information, we extract from it accurate analytical formulas for the thresholds $\phi_{1c}$ and $\phi_{2c}$ that depend on dimension $d$ and the parameter $\zeta_2$ in Sec. IV C.

### C. Percolation thresholds

By examining the behavior of Eq. (3) in the limit in which phase 2 becomes superconductive relative to phase 1, we find that approximation (3) predicts nontrivial percolation thresholds that depend on microstructural information via the parameter $\zeta_2$. Specifically, taking the limit $\sigma_2/\sigma_1 \to \infty$ in Eq. (3) yields

$$\frac{\sigma_e}{\sigma_1} = \frac{1+\phi_2+(1-d+d\phi_2-2\phi_2)\zeta_2}{1+\phi_2+(1-d-2\phi_2)\zeta_2+d\phi_2(\zeta_2-1)}. \quad (8)$$

Henceforth, we estimate the value of the threshold $\phi_{2c}$ from Eq. (8) in terms of $\zeta_2$ and $d$ by setting the denominator of Eq. (8) to zero and solving for $\phi_2$ [1], finding that

$$\phi_{2c} = \frac{(d-1)\zeta_2 - 1}{1-d+(d-2)\zeta_2}, \quad (9)$$

in which $\zeta_2$ is implicitly a function of $\phi_2$. Note that there are no limitations on the value of $\zeta_2$ in Eq. (9) in 2D, while one must have $\zeta_2 \leqslant \frac{1}{2}$ in 3D. We find that Eq. (9) predicts that all 2D phase-inversion symmetric microstructures have threshold $\phi_{2c} = \frac{1}{2}$ which is consistent with observations in previous work [1,65,66]. In the case of 3D symmetric-cell materials, Eq. (9) predicts

$$\phi_{2c}(g) = \frac{-4+5g+\sqrt{12-24g+9g^2}}{4g-2}, \qquad g < \frac{1}{2}. \quad (10)$$

It is also fruitful to examine the behavior of approximation (3) in the limit in which phase 2 becomes insulating relative to phase 1. Taking the limit $\sigma_2/\sigma_1 \to 0$ in Eq. (3), we find that

$$\frac{\sigma_e}{\sigma_1} = \frac{1+\phi_2+(1-2\phi_2)\zeta_2+d(\phi_2\zeta_2-1)}{1+\phi_2+(1-2\phi_1)\zeta_2+d[\phi_2(1-\zeta_2)-1]}. \quad (11)$$

By ascertaining the value of $\phi_2$ in which approximation (11) goes to zero, we can determine when phase 1 becomes disconnected and thus predict the phase 1 percolation threshold $\phi_{1c}$. We specifically find that

$$\phi_{1c} = 1 - \frac{d-\zeta_2-1}{1+(d-2)\zeta_2}, \quad (12)$$

in which $\zeta_2$ is implicitly a function of $\phi_2$. Note that there are no limits on the value of $\zeta_2$ in Eq. (12) in 2D, while one must have $\zeta_2 \geqslant \frac{1}{2}$ in 3D. Taken together, Eqs. (9) and (12) can be used to predict the range of volume fractions over which a microstructure is bicontinuous. For 2D systems, we find that $\phi_{2c} = 1 - \phi_{1c}$, implying that there is no bicontinuity of phases in this dimension. By contrast, these equations generally predict that 3D microstructures will be bicontinuous for $\phi_{2c} < \phi_2 < 1 - \phi_{1c}$.

Values of $\phi_{2c}$ and $\phi_{1c}$ for the 2D and 3D models as predicted by formulas (9) and (12), respectively, as well as thresholds obtained via simulation methods are listed in Table I. See Appendix B for details on how we estimated the value of $\phi_{2c}$ for 3D DRM. We find good quantitative agreement between the predicted and numerically obtained thresholds for the phase-inversion symmetric models. Additionally, despite the fully penetrable particle models not being phase-inversion symmetric, the values of $\phi_{2c}$ and $\phi_{1c}$ predicted via formulas (9) and (12) for these systems are in good quantitative and/or qualitative agreement with the numerically obtained thresholds. Moreover, the theoretically predicted and actual intervals of volume fractions in which the 3D models are bicontinuous are in good qualitative and/or quantitative agreement with one another.

The incorporation of nontrivial phase clustering information into Eq. (3) across dimensions is further highlighted in the plots of this approximation in the superconducting and insulating limits [i.e., Eqs. (8) and (11), respectively] as functions of $\phi_2$ for 2D Debye random media and fully penetrable disks in Fig. 7(a) and 3D Debye random media and fully penetrable spheres in Fig. 7(b). For each model microstructure, we specifically observe that Eq. (8) diverges to infinity (i.e., the composite becomes superconductive) precisely when phase 2 forms as a sample spanning cluster at the threshold predicted by Eq. (9). By contrast, Eq. (11) abruptly drops to zero (i.e., the composite becomes insulating) when phase 1 becomes disconnected, as predicted by Eq. (12). Finally, the nontrivial ranges of volume fractions over which these 3D microstructures are predicted to be bicontinuous are highlighted by the different volume fractions at which they are predicted to become superconducting and insulating, as seen in Fig. 7(b).

## V. DISCUSSION AND CONCLUSIONS

In summary, we have shown via comprehensive numerical simulations that the self-consistent strong-contrast approximation (3) accurately predicts the effective conductivities of four model disordered microstructures in which both phases

TABLE I. Values of the percolation thresholds $\phi_{2c}$ and $\phi_{1c}$ for the model microstructures as predicted by formulas (9) and (12), respectively, as well as those obtained using numerical simulations. The lower limits on the thresholds for the RCB systems correspond to site percolation when connections between nearest neighbors and next-nearest neighbors are considered. By contrast, the upper limits correspond to site percolation when only nearest-neighbor connections are considered. Good qualitative and/or quantitative agreement is seen between the theoretically predicted and known values of the thresholds. Note that these calculations take the matrix and particle phases of the fully penetrable particle models to be phases 1 and 2, respectively.

| Model | $\phi_{2c}$, Eq. (9) | $\phi_{2c}$, actual | $\phi_{1c}$, Eq. (12) | $\phi_{1c}$, actual |
|---|---|---|---|---|
| Random checkerboard (2D) | 0.500 | $0.407 \leqslant \phi_{2c} \leqslant 0.593$ [1] | 0.500 | $0.407 \leqslant \phi_{1c} \leqslant 0.593$ [1] |
| Random checkerboard (3D) | 0.236 | $0.199 \leqslant \phi_{2c} \leqslant 0.312$ [76] | 0.236 | $0.199 \leqslant \phi_{1c} \leqslant 0.312$ [76] |
| Debye random media (2D) | 0.500 | 0.500 [65,66] | 0.500 | 0.500 [65,66] |
| Debye random media (3D) | 0.182 | 0.115 (Appendix B) | 0.182 | 0.115 (Appendix B) |
| Fully penetrable disks | 0.609 | 0.676 [77] | 0.391 | 0.324 [77] |
| Fully penetrable spheres | 0.337 | 0.289 [78] | 0.078 | 0.030 [79] |
| Fully penetrable ellipses ($b/a = 5$) | 0.420 | 0.460 [80] | 0.580 | 0.540 [80] |
| Fully penetrable oblate ellipsoids ($b/a = 5$) | 0.094 | 0.176 [81] | 0.194 | 0.094[a] [82] |

[a]This value of $\phi_{1c}$ was extrapolated from values of the phase 1 percolation thresholds for fully penetrable oblate ellipsoid systems with other aspect ratios $b/a$ that were ascertained in Ref. [82].

form large, well-connected clusters in 2D and 3D across phase volume fractions. Additionally, Eq. (3) always lies between the tightest three-point bounds under the specified conditions described in Appendix A. Moreover, the accuracy of Eq. (3) is attributable to its prediction of nontrivial percolation thresholds that incorporate $\zeta_2$ that were found to be in good quantitative and/or qualitative agreement with the known thresholds for the aforementioned models.

One potentially fruitful area of future research is to derive an approximation analogous to Eq. (3) that accurately predicts the effective stiffness tensor $\mathbf{C}_e$ of phase-inversion symmetric materials. Such a derivation would likely involve the strong-contrast expansion for $\mathbf{C}_e$ derived in Ref. [22]. It is also an outstanding problem to ascertain precise percolation thresholds for 3D Debye random media as well as other model phase-inversion symmetric microstructures (like those examined in Ref. [83]) to more comprehensively test the accuracy of $\phi_{2c}$ predicted by Eq. (10). Such calculations are challenging, as they require the computationally intensive generation of many large realizations of microstructures with prescribed two-point correlation functions [65,84].

Finally, we note that approximation (3) could be used to guide an inverse design problem in which microstructures with prescribed $\sigma_e$ for a given volume fraction are realized by symmetric-cell materials with targeted cell-shape parameters $g$. For simplicity, one could target tessellations of polydisperse elliptical or ellipsoidal cells whose shape parameters $g$ can be determined exactly in terms of their aspect ratios [1]. These microstructures could be effectively realized computationally by an adaptation of the tessellation-based procedure of Kim and Torquato [63,64]. Finally, self-supporting microstructures, which could be manufactured by 3D printing techniques [85], could be targeted in this scheme by ensuring the volume fraction of phase 2 of the designed microstructures is sufficiently above the percolation threshold as determined by Eq. (10).

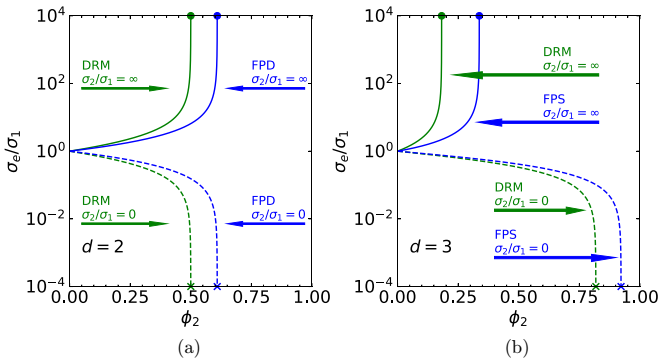



FIG. 7. Log-linear plots of the scaled effective conductivity $\sigma_e/\sigma_1$ as a function of phase 2 volume fraction $\phi_2$ as predicted by Eqs. (8) and (11) for (a) 2D Debye random media and fully penetrable disks and (b) 3D Debye random media and fully penetrable spheres. Solid lines correspond to formula (8) in which phase 2 is superconducting, while dashed lines correspond to formula (11) in which phase 2 is insulating. In (a) and (b), the circles and x's mark the locations of $\phi_{2c}$ predicted by Eq. (9) and $1 - \phi_{1c}$ predicted by Eq. (12), respectively, for these models.

## ACKNOWLEDGMENTS

This paper was sponsored by the Army Research Office and was accomplished under Cooperative Agreement No. W911NF-22-2-0103. M.S. also acknowledges the support of the Harold W. Dodds Honorific Fellowship. The authors thank the Princeton Institute for Computational Science and Engineering for the computational resources.

## DATA AVAILABILITY

The data that support the findings of this article are not publicly available. The data are available from the authors upon reasonable request.

## APPENDIX A: RESTRICTING THE SELF-CONSISTENT STRONG-CONTRAST APPROXIMATION BETWEEN THREE-POINT BOUNDS

We will require that approximation (3) always lies between the most restrictive three-point bounds on the effective conductivity, i.e., the three-point Beran-type lower and upper

TABLE II. Ranges of $\phi_2$ values in which approximation (3) for the 3D models considered here with $\gamma = 10$ should lie between the three-point bounds (A1) and (A2) as determined by Eq. (A4) and the constraints in Eq. (A3).

| 3D model | Ranges of valid $\phi_2$ values for $\gamma = 10$ |
|---|---|
| RCB | $0 < \phi_2 < \frac{1}{2}, \phi_2 \gtrsim 0.93$ |
| DRM | $0 < \phi_2 < \frac{1}{2}, \phi_2 \gtrsim 0.85$ |
| FPS | $0 < \phi_2 < \frac{1}{2}, \phi_2 \gtrsim 0.70$ |
| FPE | $0 < \phi_2 < \frac{1}{2}, \phi_2 \gtrsim 0.82$ |

bounds which are given by [1,44–46,48,86,87]

$$\sigma_L^{(3)} = \langle\sigma\rangle - \frac{\phi_1\phi_2(\sigma_2-\sigma_1)^2}{\langle\tilde{\sigma}\rangle + (d-1)\langle\sigma^{-1}\rangle_\zeta^{-1}}, \tag{A1}$$

and

$$\sigma_U^{(3)} = \langle\sigma\rangle - \frac{\phi_1\phi_2(\sigma_2-\sigma_1)^2}{\langle\tilde{\sigma}\rangle + (d-1)\langle\sigma\rangle_\zeta}, \tag{A2}$$

respectively. Note that $\langle\sigma\rangle = \phi_1\sigma_1 + \phi_2\sigma_2$, $\langle\tilde{\sigma}\rangle = \phi_2\sigma_1 + \phi_1\sigma_2$, and $\langle c\rangle_\zeta = c_1\zeta_1 + c_2\zeta_2$. By incorporating three-point microstructural information via the parameter $\zeta_2$, these bounds improve upon the well-known Hashin-Shtrikman lower and upper bounds [88,89]. Placing such a requirement on Eq. (3) will generally restrict the range of values of $\zeta_2$ beyond the normal condition that it must lie in the interval $[0, 1]$ [1]. Following Torquato [32], we use the so-called Y-transformation [90,91] to determine that formula (3) lies between bounds (A1) and (A2) for $0 \leqslant \zeta_2 \leqslant 1$ for 2D microstructures. Repeating the same procedure for 3D systems, we find that Eq. (3) lies between the three-point bounds provided that

$$\begin{aligned} &0 < \zeta_2 < \tfrac{1}{2} \quad \text{and} \quad \phi_2 < f(\zeta_2, \gamma) \\ &\tfrac{1}{2} < \zeta_2 < 1 \quad \text{and} \quad \phi_2 > f(\zeta_2, \gamma), \end{aligned} \tag{A3}$$

in which $\gamma = \sigma_2/\sigma_1$ and

$$f(\zeta_2,\gamma) = \frac{\zeta_2(1+2\gamma)[2(1-\zeta_2)+(2\zeta_2+1)\gamma]}{2\left(\zeta_2^2-4\zeta_2+3\right)+\left(-4\zeta_2^2+4\zeta_2+3\right)\gamma+2\zeta_2(\zeta_2+2)\gamma^2}. \tag{A4}$$

We calculate the ranges of valid $\phi_2$ for the 3D models considered here for $\gamma = 10$ via the conditions (A3) and (A4) and list them in Table II. For these models, the range of $\phi_2$ values in which Eq. (3) violates the bounds (i.e., $\frac{1}{2} < \phi_2 \lesssim 0.93$) coincides with that in which the approximation has the largest percent error as compared with simulation, as seen in Fig. 5(b) and described in Sec. IV.

## APPENDIX B: ESTIMATING THE PERCOLATION THRESHOLD OF 3D DEBYE RANDOM MEDIA

In order to test the accuracy of the percolation thresholds $\phi_{2c}$ predicted via Eq. (8) for 3D Debye random media, we estimate here the value of $\phi_{2c}$ for this model. For each volume fraction $\phi_2$, we specifically search for sample-spanning clusters in 20 different realizations of $192 \times 192 \times 192$ voxel 3D DRM. To identify such clusters, we use the burning algorithm [92] and consider only nearest-neighbor voxel connections for simplicity. We find that the fraction of configurations supporting percolating clusters $f_p = 0$ for $\phi_2 = 0.08$, while $f_p = 1$ for $\phi_2 = 0.15$, with $f_p$ increasing with $\phi_2$ for $0.08 < \phi_2 < 0.15$. As narrowing the range of volume fractions in which $\phi_{2c}$ lies requires the computationally expensive generation of additional, larger configurations, here, we estimate $\phi_{2c}$ to be the median of this interval, i.e., $\phi_{2c} = (0.08 + 0.15)/2 = 0.115$. This estimated threshold is reasonably close to $\phi_{2c} = 0.182$, as predicted via Eq. (8) for this model. The percolating network of a $\phi_2 = 0.15$ realization of 3D DRM is highlighted in Fig. 8.

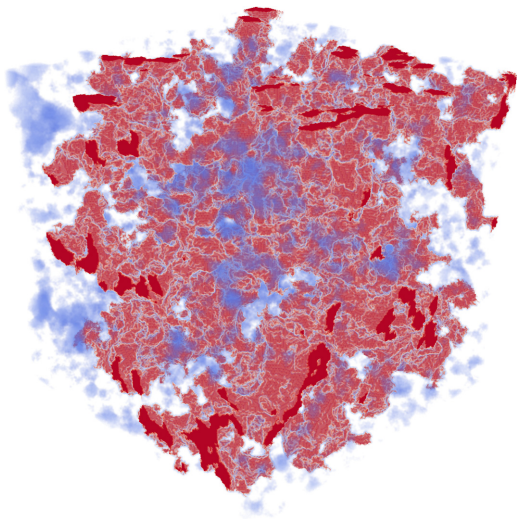


FIG. 8. A realization of 3D Debye random media at $\phi_2 = 0.15$ with its percolating cluster of phase 2 highlighted in red. The nonpercolating domains of phase 2 are highlighted in blue, while phase 1 is transparent to facilitate visualization. The image shown here corresponds to the entire $192 \times 192 \times 192$ voxel sample.

[1] S. Torquato, *Random Heterogeneous Materials: Microstructure and Macroscopic Properties* (Springer-Verlag, New York, 2002).

[2] M. Sahimi, *Heterogeneous Materials I: Linear Transport and Optical Properties* (Springer-Verlag, New York, 2003).

[3] G. W. Milton, *The Theory of Composites* (Cambridge University Press, Cambridge, 2002).

[4] B. Patel and T. I. Zohdi, Numerical estimation of effective electromagnetic properties for design of particulate composites, Mater. Des. **94**, 546 (2016).

[5] S. Torquato, Morphology and effective properties of disordered heterogeneous media, Int. J. Solids Struct. **35**, 2385 (1998).

[6] A. Chremos and J. F. Douglas, Particle localization and hyperuniformity of polymer-grafted nanoparticle materials, Ann. Phys. **529**, 1600342 (2017).

[7] A. Chremos and J. F. Douglas, Hidden hyperuniformity in soft polymeric materials, Phys. Rev. Lett. **121**, 258002 (2018).

[8] M. Huang, W. Hu, S. Yang, Q.-X. Liu, and H. Zhang, Circular swimming motility and disordered hyperuniform state in an algae system, Proc. Natl. Acad. Sci. USA **118**, e2100493118 (2021).

[9] C. J. Brinker and G. W. Scherer, *Sol-Gel Science: The Physics and Chemistry of Sol-Gel Processing* (Academic Press, New York, 1990).

[10] A. P. Roberts, Morphology and thermal conductivity of model organic aerogels, Phys. Rev. E **55**, R1286 (1997).

[11] L. Poladian, Effective transport and optical properties of composite materials, Ph.D. Thesis, University of Sydney, Australia, 1990.

[12] S. Torquato, I. C. Kim, and D. Cule, Effective conductivity, dielectric constant, and diffusion coefficient of digitized composite media via first-passage-time equations, J. Appl. Phys. **85**, 1560 (1999).

[13] J. Bauer, M. Sala-Casanovas, M. Amiri, and L. Valdevit, Nanoarchitected metal/ceramic interpenetrating phase composites, Sci. Adv. **8**, eabo3080 (2022).

[14] Y. Jung and S. Torquato, Fluid permeabilities of triply periodic minimal surfaces, Phys. Rev. E **72**, 056319 (2005).

[15] Y. Zhang, M.-T. Hsieh, and L. Valdevit, Mechanical performance of 3D printed interpenetrating phase composites with spinodal topologies, Compos. Struct. **263**, 113693 (2021).

[16] S. Torquato and J. Kim, Microstructural and transport characteristics of triply periodic bicontinuous materials, Acta Mater. **276**, 120142 (2024).

[17] A. Selkirk, N. Prochukhan, R. Lundy, C. Cummins, R. Gatensby, R. Kilbride, A. Parnell, J. Baez Vasquez, M. Morris, and P. Mokarian-Tabari, Optimization and control of large block copolymer self-assembly via precision solvent vapor annealing, Macromolecules **54**, 1203 (2021).

[18] M.-T. Hsieh, B. Endo, Y. Zhang, J. Bauer, and L. Valdevit, The mechanical response of cellular materials with spinodal topologies, J. Mech. Phys. Solids **125**, 401 (2019).

[19] J. W. Cahn and J. E. Hilliard, Free energy of a nonuniform system. I. Interfacial free energy, J. Chem. Phys. **28**, 258 (1958).

[20] J. W. Cahn, Phase separation by spinodal decomposition in isotropic systems, J. Chem. Phys. **42**, 93 (1965).

[21] A. K. Sen and S. Torquato, Effective conductivity of anisotropic two-phase composite media, Phys. Rev. B **39**, 4504 (1989).

[22] S. Torquato, Exact expression for the effective elastic tensor of disordered composites, Phys. Rev. Lett. **79**, 681 (1997).

[23] J. Kim and S. Torquato, Effective elastic wave characteristics of composite media, New J. Phys. **22**, 123050 (2020).

[24] S. Torquato and J. Kim, Nonlocal effective electromagnetic wave characteristics of composite media: Beyond the quasistatic regime, Phys. Rev. X **11**, 021002 (2021).

[25] J. Kim and S. Torquato, Multifunctional composites for elastic and electromagnetic wave propagation, Proc. Natl. Acad. Sci. USA **117**, 8764 (2020).

[26] S. Torquato, Effective electrical conductivity of two-phase disordered composite media, J. Appl. Phys. **58**, 3790 (1985).

[27] S. Torquato, Effective stiffness tensor of composite media: I. Exact series expansions, J. Mech. Phys. Solids **45**, 1421 (1997).

[28] W. F. Brown, Solid mixture permittivities, J. Chem. Phys. **23**, 1514 (1955).

[29] D. J. Bergman, The dielectric constant of a composite material—A problem in classical physics, Phys. Rep. **43**, 377 (1978).

[30] D. J. Bergman, Dielectric constant of a two-component granular composite: A practical scheme for calculating the pole spectrum, Phys. Rev. B **19**, 2359 (1979).

[31] G. W. Milton, Multicomponent composites, electrical networks and new types of continued fractions. I and II, Commun. Math. Phys. **111**, 281 (1987).

[32] S. Torquato, Effective stiffness tensor of composite media: II. Applications to isotropic dispersions, J. Mech. Phys. Solids **46**, 1411 (1998).

[33] A. Gillman and K. Matouš, Third-order model of thermal conductivity for random polydisperse particulate materials using well-resolved statistical descriptions from tomography, Phys. Lett. A **378**, 3070 (2014).

[34] M. Skolnick and S. Torquato, Effective transport and mechanical properties of two-phase materials across the order-disorder spectrum, Acta Mater. **290**, 120921 (2025).

[35] A. Gillman, G. Amadio, K. Matouš, and T. L. Jackson, Third-order thermo-mechanical properties for packs of Platonic solids using statistical micromechanics, Proc. R. Soc. Lond. A **471**, 20150060 (2015).

[36] F. Gritti and G. Guiochon, Diffusion models in chromatographic columns packed with fully and superficially porous particles, Chem. Eng. Sci. **66**, 3773 (2011).

[37] F. Gritti and G. Guiochon, Theoretical investigation of diffusion along columns packed with fully and superficially porous particles, J. Chromatogr. A **1218**, 3476 (2011).

[38] G. Desmet, K. Broeckhoven, S. Deridder, and D. Cabooter, Review of recent insights in the measurement and modelling of the B-term dispersion and related mass transfer properties in liquid chromatography, Anal. Chim. Acta **1214**, 339955 (2022).

[39] Bicontinuous microstructures are those in which both phases are topologically connected across the sample. This topological feature (i.e., percolation of both phases) is common in 3D systems but is rare in 2D ones [1].

[40] P. Debye, H. R. Anderson, and H. Brumberger, Scattering by an inhomogeneous solid. II. The correlation function and its applications, J. Appl. Phys. **28**, 679 (1957).

[41] C. L. Y. Yeong and S. Torquato, Reconstructing random media, Phys. Rev. E **57**, 495 (1998).

[42] M. J. Beran and J. Molyneux, Use of classical variational principles to determine bounds for the effective bulk modulus in heterogeneous media, Quart. Appl. Math. **24**, 107 (1966).

[43] J. J. McCoy, On the displacement field in an elastic medium with random variation of material properties, in *Recent Advances in Engineering Sciences*, Vol. 5 (Gordon and Breach, New York, 1970).

[44] N. Silnutzer, Effective constants of statistically homogeneous materials, Ph.D. Thesis, University of Pennsylvania, Philadelphia, 1972.

[45] K. Schulgasser, On the conductivity of fiber reinforced materials, J. Math. Phys. **17**, 382 (1976).

[46] S. Torquato, Microscopic approach to transport in two-phase random media, Ph.D. Thesis, State University of New York at Stony Brook, 1981.
[47] G. W. Milton, Bounds on the transport and optical properties of a two-component composite material, J. Appl. Phys. **52**, 5294 (1981).
[48] G. W. Milton, Bounds on the elastic and transport properties of two-component composites, J. Mech. Phys. Solids **30**, 177 (1982).
[49] G. W. Milton and N. Phan-Thien, New bounds on effective elastic moduli of two-component materials, Proc. R. Soc. Lond. A **380**, 305 (1982).
[50] N. Phan-Thien and G. W. Milton, New bounds on the effective thermal conductivity of $n$-phase materials, Proc. R. Soc. Lond. A **380**, 333 (1982).
[51] G. W. Milton, Correlation of the electromagnetic and elastic properties of composites and microgeometries corresponding with effective medium approximations, in *Physics and Chemistry of Porous Media*, edited by D. L. Johnson and P. N. Sen (AIP, New York, 1984).
[52] L. V. Gibiansky and S. Torquato, Geometrical-parameter bounds on effective moduli of composites, J. Mech. Phys. Solids **43**, 1587 (1995).
[53] L. V. Gibiansky and S. Torquato, Rigorous link between the conductivity and elastic moduli of fibre-reinforced composite materials, Phil. Trans. R. Soc. Lond. A **353**, 243 (1995).
[54] S. Torquato, Predicting transport characteristics of hyperuniform porous media via rigorous microstructure-property relations, Adv. Water Resour. **140**, 103565 (2020).
[55] M. A. Klatt, R. M. Ziff, and S. Torquato, Critical pore radius and transport properties of disordered hard-and overlapping-sphere models, Phys. Rev. E **104**, 014127 (2021).
[56] T. K. Tokunaga, Porous media gas diffusivity from a free path distribution model, J. Chem. Phys. **82**, 5298 (1985).
[57] S. Torquato and G. Stell, Microstructure of two-phase random media: V. The $n$-point matrix probability functions for impenetrable spheres, J. Chem. Phys. **82**, 980 (1985).
[58] S. Torquato and G. Stell, Bounds on the effective thermal conductivity of a dispersion of fully penetrable spheres, Int. J. Eng. Sci. **23**, 375 (1985).
[59] S. Torquato, G. Stell, and J. Beasley, Third-order bounds on the effective bulk and shear moduli of a dispersion of fully penetrable spheres, Int. J. Eng. Sci. **23**, 385 (1985).
[60] S. Torquato, Bulk properties of two-phase disordered media: II. Effective conductivity of a dilute dispersion of penetrable spheres, J. Chem. Phys. **83**, 4776 (1985).
[61] P. A. Smith and S. Torquato, Computer simulation results for bounds on the effective conductivity of composite media, J. Appl. Phys. **65**, 893 (1989).
[62] M. N. Miller, Bounds for effective electrical, thermal, and magnetic properties of heterogeneous materials, J. Math. Phys. **10**, 1988 (1969).
[63] J. Kim and S. Torquato, New tessellation-based procedure to design perfectly hyperuniform disordered dispersions for materials discovery, Acta Mater. **168**, 143 (2019).
[64] J. Kim and S. Torquato, Methodology to construct large realizations of perfectly hyperuniform disordered packings, Phys. Rev. E **99**, 052141 (2019).
[65] Z. Ma and S. Torquato, Generation and structural characterization of Debye random media, Phys. Rev. E **102**, 043310 (2020).
[66] M. Skolnick and S. Torquato, Understanding degeneracy of two-point correlation functions via Debye random media, Phys. Rev. E **104**, 045306 (2021).
[67] D. A. Coker, S. Torquato, and J. H. Dunsmuir, Morphology and physical properties of Fontainebleau sandstone via a tomographic analysis, J. Geophys. Res. **101**, 17497 (1996).
[68] C. Vargel, A. Royer, O. St-Jean-Rondeau, G. Picard, A. Roy, V. Sasseville, and A. Langlois, Arctic and subarctic snow microstructure analysis for microwave brightness temperature simulations, Remote Sens. Environ. **242**, 111754 (2020).
[69] C. J. Gommes, Stochastic models of disordered mesoporous materials for small-angle scattering analysis and more, Microporous Mesoporous Mater. **257**, 62 (2018).
[70] S. Torquato and G. Stell, Microstructure of two-phase random media: III. The $n$-point matrix probability functions for fully penetrable spheres, J. Chem. Phys. **79**, 1505 (1983).
[71] S. Torquato, Bulk properties of two-phase disordered media: III. New bounds on the effective conductivity of dispersions of penetrable spheres, J. Chem. Phys. **84**, 6345 (1986).
[72] We note that the self-consistent approximation for the effective conductivity [1], i.e., $\sigma_e = (\alpha + \sqrt{\alpha^2 + 4(d-1)\sigma_1\sigma_2})/2(d-1)$, in which $\alpha \equiv \sigma_1(d\phi_1 - 1) + \sigma_2(d\phi_2 - 1)$, is phase-inversion symmetric in the sense that it is invariant under swapping of the phase labels (i.e., $1 \to 2$ and $2 \to 1$). This property is to be distinguished from microstructure phase-inversion symmetry defined by relation (7).
[73] D. Stoyan, W. S. Kendall, and J. Mecke, *Stochastic Geometry and Its Applications*, 2nd ed. (Wiley, New York, 1995).
[74] M. Leuschner and F. Fritzen, Fourier-accelerated nodal solvers (FANS) for homogenization problems, Comput. Mech. **62**, 359 (2017).
[75] A. M. Dykhne, Conductivity of a two-dimensional two-phase system, Sov. Phys. JETP **32**, 63 (1971).
[76] C. D. Lorenz and R. M. Ziff, Precise determination of the bond percolation thresholds and finite-size scaling corrections for the sc, fcc, and bcc lattices, Phys. Rev. E **57**, 230 (1998).
[77] J. Quintanilla, S. Torquato, and R. M. Ziff, Efficient measurement of the percolation threshold for fully penetrable discs, J. Phys. A **33**, L399 (2000).
[78] M. D. Rintoul and S. Torquato, Precise determination of the critical threshold and exponents in a three-dimensional continuum percolation model, J. Phys. A: Math. Gen. **30**, L585 (1997).
[79] D. J. Priour, Jr. and N. J. McGuigan, Percolation through voids around randomly oriented polyhedra and axially symmetric grains, Phys. Rev. Lett. **121**, 225701 (2018).
[80] W. Xia and M. F. Thorpe, Percolation properties of random ellipses, Phys. Rev. A **38**, 2650 (1988).
[81] E. J. Garboczi, K. A. Snyder, J. F. Douglas, and M. F. Thorpe, Geometrical percolation threshold of overlapping ellipsoids, Phys. Rev. E **52**, 819 (1995).
[82] I. L. Novak, F. Gao, P. Kraikivski, and B. M. Slepchenko, Diffusion amid random overlapping obstacles: Similarities, invariants, approximations, J. Chem. Phys. **134**, 154104 (2011).
[83] S. Torquato, M. Skolnick, and J. Kim, Local order metrics for two-phase media across length scales, J. Phys. A: Math. Theor. **55**, 274003 (2022).

[84] D. Chen and S. Torquato, Designing disordered hyperuniform two-phase materials with novel physical properties, Acta Mater. **142**, 152 (2018).

[85] S. F. S. Shirazi, S. Gharehkhani, M. Mehrali, H. Yarmand, H. S. C. Metselaar, N. A. Kadri, and N. A. A. Osman, A review on powder-based additive manufacturing for tissue engineering: Selective laser sintering and inkjet 3D printing, Sci. Tech. Adv. Mater. **16**, 033502 (2015).

[86] M. Beran, Use of the variational approach to determine bounds for the effective permittivity in random media, Nuovo Cim **38**, 771 (1965).

[87] G. W. Milton, Bounds on the complex permittivity of a two-component composite material, J. Appl. Phys. **52**, 5286 (1981).

[88] Z. Hashin and S. Shtrikman, A variational approach to the theory of the effective magnetic permeability of multiphase materials, J. Appl. Phys. **33**, 3125 (1962).

[89] Z. Hashin, Theory of composite materials, in *Mechanics of Composite Materials* (Pergamon Press, New York, 1970).

[90] G. W. Milton, Composite materials with Poisson ratios close to −1, J. Mech. Phys. Solids **40**, 1105 (1992).

[91] A. V. Cherkaev and L. V. Gibiansky, The exact coupled bounds for effective tensors of electrical and magnetic properties of two-component two-dimensional composites, Proc. R. Soc. Edinburgh A **122**, 93 (1992).

[92] D. Stauffer and A. Aharony, *Introduction to Percolation Theory* (Taylor and Francis, London, 1992).